

Polar polarization A new method for polarimetry analysis

D. Izraeli,^{a,1} I. Mardor,^{a,b} E. O. Cohen,^a M. Duer,^a T. Y. Izraeli,^c I. Korover,^{a,d} J. Lichtenstadt,^a
and E. Piasezky^a

^a*School of Physics and Astronomy, Tel Aviv University, Tel Aviv 6997801, Israel.*

^b*Soreq NRC, Yavne 81800, Israel.*

^c*Guardian Optical Technologies, Derech Hashalom 7, Tel Aviv 6789208, Israel.*

^d*Department of Physics, NRCN, P.O. Box 9001, Beer-Sheva 8419001, Israel.*

E-mail: davidizraeli@post.tau.ac.il

ABSTRACT: We present a novel analysis method for measurements of polarization transferred in $A(\vec{e}, e'\vec{N})$ experiments, which can be applied to other kinds of polarization measurements as well. In this method the polarization transfer components are presented in spherical coordinates using an efficient likelihood numerical maximization based on an analytic derivation. We also propose a formalism that accounts for multi-parameter models, and which yields a smooth and continuous representation of the data (rather than using standard binning). Applying this method on simulated data generates results with reduced statistical and systematic uncertainties and enables revealing physical information that is lost in standard binning of the data. The obtained results can be compared easily to theoretical models and other measurements. Furthermore, CPU time is significantly reduced using this method.

¹Corresponding author.

Contents

1	Introduction	2
2	The method	3
2.1	Polarization estimation through maximum likelihood	3
2.1.1	Exact formalism	3
2.1.2	Analytical approximation	6
2.2	The choice of a coordinate system	7
2.2.1	Motivation for using spherical coordinates	7
2.2.2	The formalism in spherical coordinates	8
2.3	Varying polarization	9
2.3.1	Binned likelihood	10
2.3.2	Piecewise continuous linear dependence	11
2.3.3	Cubic spline interpolation weighting	11
2.4	Comparison of the data to theoretical models and other measurements	14
2.4.1	Quantifying the difference between measurements and a theoretical model	15
2.4.2	Tests of statistical consistency between measurements and calculations (p -value)	16
2.4.3	Plotting model predictions with data	17
2.4.4	Comparisons between measured results from two experiments	17
2.5	Combining the method's tools	19
3	Validity and advantages of the method	19
3.1	Simulation of a constant polarization	20
3.1.1	Generation of simulated events	20
3.1.2	Results of the method applied to simulated events with constant polarization	20
3.2	Simulation of events with varying polarization	23
3.2.1	Simulation and results	23
3.2.2	Documented source code notebook	24
4	Summary and Conclusions	24
A	Full Example	26
A.1	Derivation	26
A.2	Algorithm	27
	References	29

1 Introduction

Polarization is an important example of an observable extracted from an ensemble of events, which cannot be obtained from a single one. Other examples include half-life of unstable particles, and the mass and width of resonances. Furthermore, polarization transfer may depend on several variables that do not follow a well-defined function so that the large data set is not characterized by a single value. This is in contrast to measurements such as half-life or resonance parameters, where the entire data set is described by a well-defined function and the obtained parameters characterize the entire data set.

For the case of polarization-transfer measurements via $A(\vec{e}, e'\vec{N})$, we propose an analysis method that improves the extraction of the physical content from the measurement by using a better coordinate system. We also propose to use a continuous (unbinned) presentation of the results, and reduce computation time by improving the optimization's starting point.

Polarization measurements are customarily presented in Cartesian coordinates. In these coordinates the measured components are mixed and are measured with less accuracy than the magnitude of the polarization vector and its direction [1].

Generally, when estimators depend on certain parameters, such as kinematic variables in the case of polarization-transfer, it is customary to divide the data into bins [1–3]. The widths of these bins are usually somewhat arbitrary, set to include enough data in each bin to yield a reasonable uncertainty, and to display possible variations of the physical result as a function of the binned parameter, based on prior estimation of its behavior.

By definition, binning constitutes a compromise regarding the quality of information that may be extracted from the measurement. It includes an inherent (and usually wrong) assumption that the values in each bin are independent of each other, and further, that one single physical value applies to all data within the bin. Thus it may potentially conceal real variations within the bin width and result in increased uncertainties. In addition, binning limits the ability to compare experimental data with theoretical models or with other experiments that might be binned differently.

Excessive optimization is necessary in statistical measurements, where the physical results are the estimators that maximize the likelihood function of the given observations. Such optimization might be CPU intensive, especially if the starting point is chosen indiscriminately.

We propose an analysis method that overcomes the above limitations. In this method, we extract the polarization data in polar coordinates, which naturally exhibit the polarization magnitude and angular direction. We calculate analytically a starting point for the likelihood numerical maximization, and finally, we analyze all measured data points in a continuous manner. We assume a polynomial behavior of the estimators in each bin, and match each bin to its neighbors by demanding continuity and smoothness at all bin edges.

The paper is laid out as follows: in section §2 we describe our new method. We show in section §3 its validity and effectiveness using simulated polarization results, and we summarize and conclude in section §4.

2 The method

In this chapter we describe our new method for the calculation and analysis of particle polarization. We start by reviewing the traditional method of polarization estimation through maximum likelihood, and show that the common linear approximation can be used as a first step in an efficient numerical optimization. Next we discuss the choice of coordinate system and present the estimators for polar polarization components. Afterwards, we treat the case of varying polarization. Then we present the tools for comparing measurements with theoretical calculations. At last, we demonstrate how the entire formalism can be used in a sophisticated situation.

2.1 Polarization estimation through maximum likelihood

In this section we review the traditional way of extracting polarization using the maximum likelihood method. We then show that the approximated linear likelihood can be used as an initial step of a exact numerical optimization. We further show that the derivatives required for the following steps can be derived analytically, thus reducing the computation time by approximately two orders of magnitude.

2.1.1 Exact formalism

We define the Cartesian coordinates of the polarization transferred to a proton as:

$$\mathbf{P} = (P_x, P_y, P_z). \quad (2.1)$$

The polarization measured by a focal plane polarimeter (FPP) is determined from the distribution (f) of the proton scattering azimuthal angle (ϕ_{FPP} in figure 1b), as shown in [5]. the distribution is

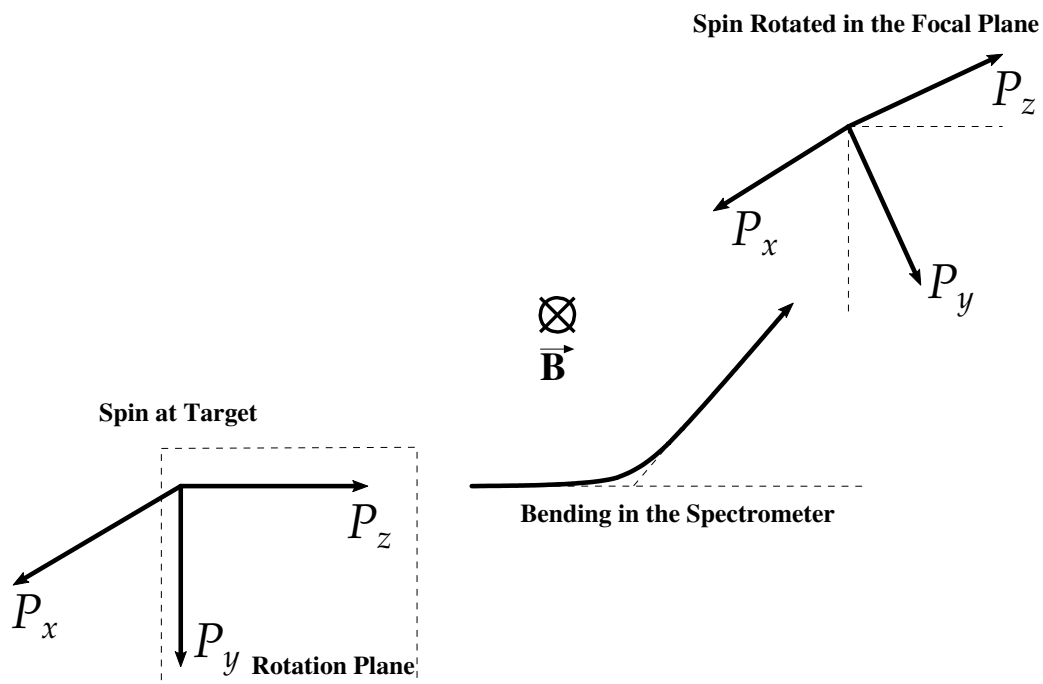
$$f(\phi_{\text{FPP}}) = \frac{1 + \gamma(\phi_{\text{FPP}})}{2\pi}, \quad (2.2)$$

where $\gamma(\phi_{\text{FPP}})$ is

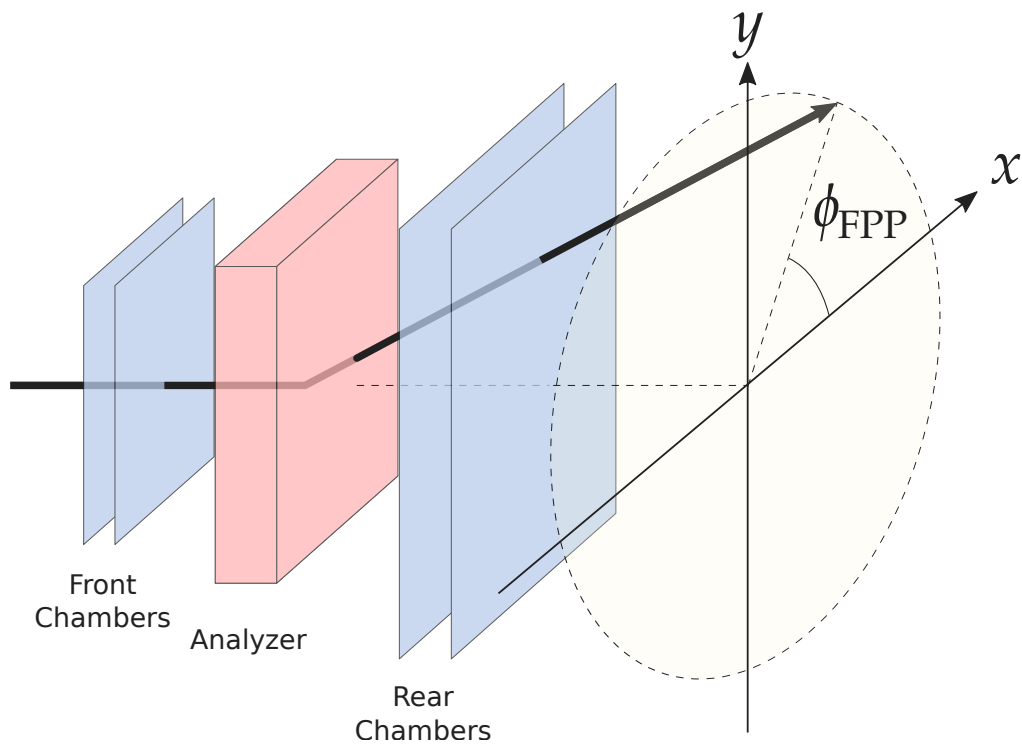
$$\begin{aligned} \gamma(\phi_{\text{FPP}}) &\equiv a \left(-\sin \phi_{\text{FPP}}, \cos \phi_{\text{FPP}}, 0 \right) \mathbf{S} \mathbf{P} \\ &= \mathbf{P} \cdot \left(a \mathbf{S}^{-1} \begin{pmatrix} -\sin \phi_{\text{FPP}} \\ \cos \phi_{\text{FPP}} \\ 0 \end{pmatrix} \right) \\ &\equiv \mathbf{P} \cdot \boldsymbol{\lambda}. \end{aligned} \quad (2.3)$$

Here $\boldsymbol{\lambda} \equiv a \mathbf{S}^{-1} \begin{pmatrix} -\sin \phi_{\text{FPP}} \\ \cos \phi_{\text{FPP}} \\ 0 \end{pmatrix} = a \begin{pmatrix} -S_{11} \sin \phi_{\text{FPP}} + S_{21} \cos \phi_{\text{FPP}} \\ -S_{12} \sin \phi_{\text{FPP}} + S_{22} \cos \phi_{\text{FPP}} \\ -S_{13} \sin \phi_{\text{FPP}} + S_{23} \cos \phi_{\text{FPP}} \end{pmatrix}$, where $S_{ij} = S_{ji}^{-1}$ are the elements of \mathbf{S} . We assume that the sought polarization \mathbf{P} is transformed to the FPP by a known spin precession matrix \mathbf{S} (see figure 1a). In addition we allow for an efficiency factor $0 < a < 1$ (usually the product of the analyzing power and the beam polarization).

We calculate the target proton polarization by obtaining its maximum likelihood estimators (MLE). To this end, we calculate the likelihood function of the target proton polarization distribution



(a) Spin precession of a proton in a spectrometer. Adapted from [2].



(b) Proton scattering azimuthal angle (ϕ_{FPP}). Adapted from [4].

Figure 1: Polarization-transfer to a proton measured by a focal plane polarimeter (FPP).

(eq. (2.2)) in the standard way:

$$\mathcal{L}(\mathbf{P}|\phi_{FPP}) = \prod_{k=1}^n (1 + \gamma_k), \quad (2.4)$$

where we omitted the constant $(2\pi)^{-n}$, with n the number of events in the sample. As is usually preferred, we continue the process with the log-likelihood function:

$$L \equiv \ln \mathcal{L} = \sum_{k=1}^n \ln(1 + \gamma_k). \quad (2.5)$$

In the following, $\nabla_{\mathbf{P}} \equiv \begin{pmatrix} \partial_{P_x} \\ \partial_{P_y} \\ \partial_{P_z} \end{pmatrix}$ is a column gradient operator, $\nabla_{\mathbf{P}}^T \equiv (\partial_{P_x}, \partial_{P_y}, \partial_{P_z})$ is a row gradient operator, and the Hessian operator is the 3×3 second derivative matrix:

$$\nabla_{\mathbf{P}} \otimes \nabla_{\mathbf{P}} \equiv \nabla_{\mathbf{P}} \nabla_{\mathbf{P}}^T = \begin{pmatrix} \partial_{P_x}^2 & \partial_{P_x} \partial_{P_y} & \partial_{P_x} \partial_{P_z} \\ \partial_{P_x} \partial_{P_y} & \partial_{P_y}^2 & \partial_{P_y} \partial_{P_z} \\ \partial_{P_x} \partial_{P_z} & \partial_{P_y} \partial_{P_z} & \partial_{P_z}^2 \end{pmatrix}. \quad (2.6)$$

We extract the MLEs of the polarization by equating the log-likelihood function's gradient to zero:

$$\begin{aligned} \nabla_{\mathbf{P}} L &= \sum_{k=1}^n \frac{\nabla_{\mathbf{P}} \gamma_k}{1 + \gamma_k} \\ &= \sum_{k=1}^n \frac{\boldsymbol{\lambda}_k}{1 + \mathbf{P} \cdot \boldsymbol{\lambda}_k} \stackrel{!}{=} 0, \end{aligned} \quad (2.7)$$

where the second expression, in terms of $\boldsymbol{\lambda}_k$, is derived using eq. (2.3) and $\nabla_{\mathbf{P}} \gamma = \boldsymbol{\lambda}$. The covariance matrix of the MLEs is given by the inverse of minus the Hessian of the log-likelihood:

$$\begin{aligned} H &\equiv \nabla_{\mathbf{P}} \otimes \nabla_{\mathbf{P}} L \\ &= \sum_{k=1}^n \left[\frac{\nabla_{\mathbf{P}} \otimes \nabla_{\mathbf{P}} \gamma_k}{1 + \gamma_k} - \left(\frac{\nabla_{\mathbf{P}} \gamma_k}{1 + \gamma_k} \right) \otimes \left(\frac{\nabla_{\mathbf{P}} \gamma_k}{1 + \gamma_k} \right) \right] \\ &= \sum_{k=1}^n \frac{-\boldsymbol{\lambda}_k \otimes \boldsymbol{\lambda}_k}{(1 + \mathbf{P} \cdot \boldsymbol{\lambda}_k)^2}. \end{aligned} \quad (2.8)$$

where again the second equality is derived using eq. (2.3) and $\nabla_{\mathbf{P}} \otimes \nabla_{\mathbf{P}} \gamma = 0$. The MLE uncertainties are [6]

$$\sigma_{P_i} = - \left[H|_{\nabla_{\mathbf{P}} L=0}^{-1} \right]_{ii}^{1/2} \quad \forall i \in \{x, y, z\}. \quad (2.9)$$

In standard analysis methods [2, 7–9], eq. (2.7) is solved numerically, with arbitrary initial guess solutions. Given the complexity of the function and the fact that in general there are no obvious good preliminary solution candidates for the numerical process, this calculation can be

CPU intensive, and might converge to a local rather than the the global maximum.

2.1.2 Analytical approximation

In order to shorten the numerical process, and ensure convergence to the correct solutions, following [5], we utilize the property $|\gamma_k| < 1$, and approximate the log-likelihood function, expanding it in γ_k up to $O(\gamma_k^3)$:

$$\begin{aligned} L &\simeq \sum_{k=1}^n \left(\gamma_k - \frac{\gamma_k^2}{2} \right) \\ &= \sum_{k=1}^n \left(\mathbf{P} \cdot \boldsymbol{\lambda}_k - \frac{(\mathbf{P} \cdot \boldsymbol{\lambda}_k)^2}{2} \right) \\ &= \mathbf{P} \cdot \mathbf{b} - \mathbf{P}^T \mathbf{J} \mathbf{P} / 2, \end{aligned} \tag{2.10}$$

where

$$\begin{aligned} b_i &\equiv \sum_{k=1}^n \lambda_{i,k}, \\ J_{ij} &\equiv \sum_{k=1}^n \lambda_{i,k} \lambda_{j,k}, \\ i, j &\in \{x, y, z\}. \end{aligned} \tag{2.11}$$

As in the previous section the connection between γ , \mathbf{P} and $\boldsymbol{\lambda}$ is given by eq. (2.3). Note that the log-likelihood finite expansion approximation is performed only in order to generate a proper set of initial solution candidates, expedite the numerical process, and ensure that a correct final solution is found to maximize L . Therefore, this approximation can be performed even in cases where γ_k is not much smaller than unity.

The first MLEs solutions are obtained by equating the gradient of the approximated log-likelihood function (eq. (2.10)) to zero. The approximate simple algebraic form leads to a linear equation:

$$\nabla_{\mathbf{P}} L \simeq \mathbf{b} - \mathbf{J} \mathbf{P} = 0, \tag{2.12}$$

and thus, the first MLE candidates (\mathbf{P}_0) are given by:

$$\mathbf{P}_0 = \mathbf{J}^{-1} \mathbf{b}. \tag{2.13}$$

We use \mathbf{P}_0 to start the numerical process of Newton–Raphson steps, defined by:

$$\mathbf{P}_i = \mathbf{P}_{i-1} - \left[H^{-1} \nabla_{\mathbf{P}} L \right]_{\mathbf{P}=\mathbf{P}_{i-1}}. \tag{2.14}$$

For $i = 1$, we insert \mathbf{P}_0 , H^{-1} and $\nabla_{\mathbf{P}} L$ from eqs. (2.13), (2.8) and (2.7), respectively, into eq. (2.14), and obtain:

$$\mathbf{P}_1 = \mathbf{P}_0 + \mathbf{J}^{-1} \mathbf{b}', \tag{2.15}$$

where \mathbf{b}' and \mathbf{J}' are defined by

$$\begin{aligned} b'_i &\equiv \sum_{k=1}^n \frac{\lambda_{i,k}}{1 + \mathbf{P}_0 \cdot \boldsymbol{\lambda}_k}, \\ J'_{ij} &\equiv \sum_{k=1}^n \frac{\lambda_{i,k} \lambda_{j,k}}{(1 + \mathbf{P}_0 \cdot \boldsymbol{\lambda}_k)^2}, \\ i, j &\in \{x, y, z\}. \end{aligned} \quad (2.16)$$

\mathbf{P}_0 and one Newton–Raphson step are good estimates, and in practice, one step is enough to reach the absolute maximum of L , limited only by the computer’s precision. In such a case the final MLEs are given by \mathbf{P}_1 . The MLEs’ covariance matrix and uncertainties are given by the inverse of minus the likelihood’s Hessian (eq. (2.8)) and eq. (2.9), respectively, both calculated at $\mathbf{P} = \mathbf{P}_1$.

2.2 The choice of a coordinate system

2.2.1 Motivation for using spherical coordinates

The above formalism is usually used in the standard Cartesian coordinates. Separate polarization components can be extracted in this way with unbiased and normally distributed MLEs, with reasonable uncertainties.

Nevertheless, many polarization-transfer experiments focus on the components ratio $R \equiv P_x/P_z$ due to technical benefit and physics interest [10]. The ratio cancels out the inherent systematic uncertainty in beam polarization and analyzing power, thus enabling the determination of R to a better precision than P_x or P_z separately. Furthermore, in the one photon exchange approximation, the elastic electron proton scattering R is proportional to the ratio of the elastic electric $G_E(Q^2)$ to the magnetic $G_M(Q^2)$ form factors at a given four-momentum transfer Q^2 [10]:

$$R_{1\text{H}} \equiv \left(\frac{P_x}{P_z} \right)_{1\text{H}} = - \frac{2M_p}{(E + E') \tan(\theta_e/2)} \cdot \frac{G_E^p(Q^2)}{G_M^p(Q^2)}, \quad (2.17)$$

where E (E') is the incident (scattered) electron energy, θ_e is the electron scattering angle, and M_p is the proton mass.

As opposed to the separate components, the MLE of R is biased, and its distribution is skewed and has fat tails. Moreover, the uncertainty in R is propagated from the relative uncertainties and covariance of P_x and P_z , and is not derived directly from the likelihood [11]:

$$\Delta R \equiv R \sqrt{\Delta P_x^2/P_x^2 + \Delta P_z^2/P_z^2 - 2 \text{Cov}[P_x, P_z]/P_x P_z}. \quad (2.18)$$

The approximation behind the propagation assumes that the relative uncertainties are small. Therefore, in small samples where the relative uncertainties are large, the propagation approximation is invalid and the formula is erroneous [6, 11]. This influences the minimal possible bin width.

To circumvent these problems, we propose to analyze the polarization in spherical coordinates, defined by:

$$\mathbf{S} = (P, \vartheta, \varphi), \quad (2.19)$$

where

$$\begin{aligned}
P^2 &\equiv P_x^2 + P_y^2 + P_z^2, \\
\rho^2 &\equiv P_y^2 + P_z^2, \\
\tan \vartheta &\equiv \rho/P_x, \\
\tan \varphi &\equiv P_y/P_z.
\end{aligned} \tag{2.20}$$

Using spherical coordinates has several advantages. First, the magnitude of the polarization vector can be extracted with higher accuracy than each of its components. Second, two independent components, the polar and azimuthal angles, do not depend on beam polarization. Third, since the polarimeter can measure only two components, in some experiments the spin precession is in the yz plane so that P_z and P_y are mixed and P_x remains unaffected by the rotation [1]. This increases the uncertainty in the measurement of R as well. In the new spherical coordinate system only the azimuthal angle (φ) is affected by the mixing. Finally, by its definition, the cotangent of the polar angle (ϑ) is very similar to R , since in elastic electron proton scattering $P_y = 0$. Therefore, $\tau \equiv \cot \vartheta$ can be related to G_E/G_M in a way similar to R . Because ϑ is derived directly, its MLE distribution is unbiased and almost normal, and its relative uncertainty is lower with respect to that of R .

2.2.2 The formalism in spherical coordinates

The MLE in spherical coordinates is defined as $S_1 \equiv S(\mathbf{P}_1)$, where $S(\mathbf{P}_1)$ is derived explicitly by the transformation given in eq. (2.20) at the value \mathbf{P}_1 (eq. (2.15)).

In principle, the covariance matrix and the uncertainties of S_1 could be derived by propagating the Cartesian uncertainties (eqs. (2.8–2.9) evaluated at \mathbf{P}_1) through the transformation of eq. (2.20). However, this would result in large uncertainties, losing the main advantages of using spherical coordinates. We therefore derive these values directly from the polarization components in spherical coordinates, as elaborated below.

The log-likelihood function (eq. (2.5)) in spherical coordinates is given by:

$$\begin{aligned}
L(\mathbf{S}) &= \sum_{k=1}^n \ln(1 + \gamma_k) \\
&= \sum_{k=1}^n \ln(1 + \lambda_{x,k} P \cos \vartheta + \lambda_{y,k} P \sin \vartheta \sin \varphi + \lambda_{z,k} P \sin \vartheta \cos \varphi).
\end{aligned} \tag{2.21}$$

As a preliminary technical step towards calculating the gradients of the log-likelihood function, for non-vanishing polarization, we first calculate the first derivatives of γ :

$$\begin{aligned}
\partial_P \gamma &= \lambda_x \cos \vartheta + \lambda_y \sin \vartheta \sin \varphi + \lambda_z \sin \vartheta \cos \varphi \\
&= \gamma/P, \\
\partial_{\vartheta} \gamma &= -\lambda_x P \sin \vartheta + \lambda_y P \cos \vartheta \sin \varphi + \lambda_z P \cos \vartheta \cos \varphi \\
&= -\lambda_x \rho + \xi \tau, \\
\partial_{\varphi} \gamma &= \lambda_y P \sin \vartheta \cos \varphi - \lambda_z P \sin \vartheta \sin \varphi
\end{aligned}$$

$$= \bar{\xi}, \quad (2.22)$$

where $\tau = \cot \vartheta$, $\xi \equiv P \sin \vartheta (\lambda_y \sin \varphi + \lambda_z \cos \varphi) = \lambda_y P_y + \lambda_z P_z$, and $\bar{\xi} \equiv P \sin \vartheta (\lambda_y \cos \varphi - \lambda_z \sin \varphi) = \lambda_y P_z - \lambda_z P_y$. These can be combined to

$$\nabla_S \gamma = \begin{pmatrix} \gamma/P \\ -\lambda_x \rho + \xi \tau \\ \bar{\xi} \end{pmatrix}. \quad (2.23)$$

The second derivatives of γ are

$$\begin{aligned} \partial_P^2 \gamma &= 0, \\ \partial_\vartheta \partial_P \gamma &= -\lambda_x \sin \vartheta + (\lambda_y \sin \varphi + \lambda_z \cos \varphi) \cos \vartheta \\ &= (\xi \tau - \lambda_x \rho) / P, \\ \partial_\varphi \partial_P \gamma &= (\lambda_y \cos \varphi - \lambda_z \sin \varphi) \sin \vartheta \\ &= \bar{\xi} / P, \\ \partial_\vartheta^2 \gamma &= -P (\lambda_x \cos \vartheta + (\lambda_y \sin \varphi + \lambda_z \cos \varphi) \sin \vartheta) \\ &= -\gamma, \\ \partial_\varphi \partial_\vartheta \gamma &= (\lambda_y \cos \varphi - \lambda_z \sin \varphi) P \cos \vartheta \\ &= \bar{\xi} \tau, \\ \partial_\varphi^2 \gamma &= (\lambda_y \sin \varphi + \lambda_z \cos \varphi) P \sin \vartheta \\ &= -\xi, \end{aligned} \quad (2.24)$$

hence

$$\nabla_S \otimes \nabla_S \gamma = \begin{pmatrix} \partial_P^2 \gamma & \partial_\vartheta \partial_P \gamma & \partial_\varphi \partial_P \gamma \\ \partial_\vartheta \partial_P \gamma & \partial_\vartheta^2 \gamma & \partial_\varphi \partial_\vartheta \gamma \\ \partial_\varphi \partial_P \gamma & \partial_\varphi \partial_\vartheta \gamma & \partial_\varphi^2 \gamma \end{pmatrix} = - \begin{pmatrix} 0 & \frac{\lambda_x \rho - \xi \tau}{P} & -\frac{\bar{\xi}}{P} \\ \frac{\lambda_x \rho - \xi \tau}{P} & \gamma & -\bar{\xi} \tau \\ -\frac{\bar{\xi}}{P} & -\bar{\xi} \tau & \xi \end{pmatrix}. \quad (2.25)$$

We further define J'' :

$$J'' \equiv -\nabla_S \otimes \nabla_S L = \sum_{k=1}^n \left[\left(\frac{\nabla_S \gamma_k}{1 + \gamma_k} \right) \otimes \left(\frac{\nabla_S \gamma_k}{1 + \gamma_k} \right) - \frac{\nabla_S \otimes \nabla_S \gamma_k}{1 + \gamma_k} \right]. \quad (2.26)$$

The estimated asymptotic covariance matrix is the inverse of J'' , and the uncertainties are given by the S equivalent of eq. (2.9), both calculated at S_1 .

2.3 Varying polarization

In the previous sections, we assumed that the polarization \mathbf{P} is constant for all of the events. In reality the polarization of each event is different, and depends on several physical variables, such as momentum transfer squared (Q^2), missing momentum, virtuality [12, 13], etc. Usually one sets up an experiment in a way that all but one of the variables are fixed, and investigates the polarization dependence on that one variable. In the following, we present our tool for extracting the polarization in this case of non-constant polarization.

In the most general case, the polarization \mathbf{P} has a different value for each event, and then log-likelihood L takes the form

$$L = \sum_{k=1}^n \ln(1 + \mathbf{P}_k \cdot \boldsymbol{\lambda}_k). \quad (2.27)$$

In this case, L has $3n$ parameters, where n is the number of events, so that the problem of extracting \mathbf{P} is under-determined. However, if the polarization depends on a certain measured variable v , the derivation of $\mathbf{P}(v)$ is possible by maximizing a generalized likelihood function, as described below.

2.3.1 Binned likelihood

The traditional way of describing the dependence of polarization data (or any other data) on a variable, is by displaying the measurement in bins of that variable. The events are divided into $N + 1$ bins¹ of the variable v , where each bin is defined by the range (v_{l-1}, v_l) . Binning is expressed mathematically by assigning a weight w_{lk} to each event k , which takes the value 1 when v is in the

bin range (v_{l-1}, v_l) and 0 otherwise, namely, $w_{lk} = \begin{cases} 1 & v_k \in (v_{l-1}, v_l) \\ 0 & v_k \notin (v_{l-1}, v_l) \end{cases}$.

The likelihood function now obtains a generalized form that includes the polarization binning in v , $\mathbf{P}(v) = \sum_{l=0}^N w_l(v) \mathbf{P}_l$, where \mathbf{P}_l are the $3(N + 1)$ parameters of $\mathbf{P}(v)$, and $w_l(v)$ are the weight functions that satisfy $w_{lk} = w_l(v_k)$.

L is now given by:

$$L = \sum_{k=1}^n \ln \left(1 + \sum_{l=0}^N w_{lk} \mathbf{P}_l \cdot \boldsymbol{\lambda}_k \right). \quad (2.28)$$

The MLE of \mathbf{P}_l and their uncertainties can be found by extending the definitions of \mathbf{b} , \mathbf{J} , \mathbf{b}' and \mathbf{J}' from eqs. (2.11) and (2.16) respectively:

$$\begin{aligned} b_{3l+i} &\equiv \sum_{k=1}^n w_{lk} \lambda_{i,k}, \\ J_{3l+i, 3l'+j} &\equiv \sum_{k=1}^n w_{lk} w_{l'k} \lambda_{i,k} \lambda_{j,k}, \\ b'_{3l+i} &\equiv \sum_{k=1}^n \frac{w_{lk} \lambda_{i,k}}{1 + \gamma_k}, \\ J'_{3l+i, 3l'+j} &\equiv \sum_{k=1}^n \frac{w_{lk} w_{l'k} \lambda_{i,k} \lambda_{j,k}}{(1 + \gamma_k)^2}, \\ i, j &\in \{x = 1, y = 2, z = 3\}, \end{aligned} \quad (2.29)$$

where $\gamma_k \equiv \sum_{l=0}^N w_{lk} \mathbf{P}_l \cdot \boldsymbol{\lambda}_k$ extends eq. (2.3).

The algebra of eqs. (2.13), (2.15) and (2.9) still holds:

$$\mathbf{P}_0 = \mathbf{J}^{-1} \mathbf{b}$$

¹We chose to divide to $N + 1$ bins rather than N , for consistency of the algebra between the binned solution and the following continuous description.

$$\mathbf{P}_1 = \mathbf{P}_0 + \mathbf{J}'^{-1} \mathbf{b}'$$

$$\sigma_{P_{1,i}} = - \left[\mathbf{J}'^{-1} \mathbf{P}_1 \right]_{ii}^{1/2} \quad \forall i \in \{x, y, z\}.$$

Since in the binned likelihood case, the weights are merely indications of whether the event is in a specific bin or not, and the parameters \mathbf{P}_l ($l = 0$ to N) are the values of \mathbf{P} in each of the $N + 1$ bins, the matrix \mathbf{J} (eq. (2.29)) now becomes a block matrix, where each block corresponds to a bin. Since by definition the polarization is constant for each bin, the results for \mathbf{P}_1 can also be extracted from each block of the matrix according to the formalism described in section 2.1.2.

As discussed in section §1, using bins is a compromise regarding the amount of physical information that may be extracted from the measurement. In the following, we present a method that also accounts for the location of each event inside the bin.

2.3.2 Piecewise continuous linear dependence

The first step of generalizing the binned approach is to assume a continuous linear dependence of the polarization within each bin². The polarization is thus defined as a piecewise continuous function $\mathbf{P}(v) = \mathbf{p}_l(v) \quad \forall v \in (v_{l-1}, v_l)$, where $\mathbf{p}_l(v)$ is a linear interpolation between the polarization at the edges, \mathbf{P}_{l-1} and \mathbf{P}_l :

$$\mathbf{p}_l(v) = \frac{v_l - v}{v_l - v_{l-1}} \mathbf{P}_{l-1} + \frac{v - v_{l-1}}{v_l - v_{l-1}} \mathbf{P}_l = (1 - x) \mathbf{P}_{l-1} + x \mathbf{P}_l \quad (2.30)$$

v_l and \mathbf{P}_l are now the values at the edges of the a-priori defined bins, and

$$x(v) \equiv \frac{v - v_{l-1}}{v_l - v_{l-1}} \quad \forall v \in (v_{l-1}, v_l) \quad (2.31)$$

is the relative position in the bin.

The weights are now continuous and linear inside the relevant bin and zero outside:

$$w_{lk} = \begin{cases} 1 - x & v_k \in (v_{l-1}, v_l) \\ x & v_k \in (v_l, v_{l+1}) \\ 0 & v_k \notin (v_{l-1}, v_{l+1}) \end{cases} \quad (2.32)$$

These weights are then inserted into eq. (2.29) to deduce the MLE values and their uncertainties.

2.3.3 Cubic spline interpolation weighting

The behavior of the measured polarization may not be limited to linear form. However, high order polynomial interpolation is susceptible to Runge's phenomenon of oscillation at the edges of the interval. Therefore, we opt to perform spline interpolation.

In interpolating problems, spline interpolation is often preferred over polynomial interpolation because it yields similar results, even when using lower degree polynomials. We outline here a derivation of the polarization via maximizing the likelihood for the commonly used cubic spline.

²Of now N bins, rather than $N + 1$ in the previous section.

A cubic spline $\mathbf{P}(v)$ with $N + 1$ knots is a piecewise function constructed of N cubic functions

$$\mathbf{p}_l(v) = \sum_{i=0}^3 \tilde{\mathbf{a}}_{il} v^i = \sum_{i=0}^3 \mathbf{a}_{il} x^i, \quad (2.33)$$

where x defines the relative position between the knots (that is, the range within the bin) as in eq. (2.31).

The parameters are the values at the knots $\mathbf{P}(v_l) = \mathbf{P}_l$. We demand C^2 continuity:

$$\mathbf{p}_l(v_l) = \mathbf{p}_{l+1}(v_l), \quad (2.34a)$$

$$\mathbf{p}'_l(v_l) = \mathbf{p}'_{l+1}(v_l), \quad (2.34b)$$

$$\mathbf{p}''_l(v_l) = \mathbf{p}''_{l+1}(v_l). \quad (2.34c)$$

We note that from here on the derivation is given for one dimension, since the weight is defined per event, so each polarization component has the same weight. Generalizing to three dimensions merely means writing the same equations three times with different component indices.

We now proceed to write explicitly all the constraints on the cubic spline coefficients a_{il} . We start by writing the expressions for p_l at the $N + 1$ knots. The first N equations are for the left edges of the respective bins ($x = 0$). Inserting $x = 0$ into eq. (2.33) one obtains:

$$p_l(v_{l-1}) = a_{0l} = P_{l-1} \quad \forall l \in (1, N). \quad (2.35)$$

The $(N + 1)$ th equation is defined at the last knot, namely the right edge ($x = 1$) of the rightmost bin. Eq. (2.33) becomes:

$$p_N(v_N) = \sum_{i=0}^3 a_{i,N} = P_N. \quad (2.36)$$

We can combine these $N + 1$ equations into the matrix equation $\mathbf{A}_P \vec{\mathbf{a}} = \vec{\mathbf{P}}$, where

$$\begin{aligned} \mathbf{A}_P &\equiv \left(\begin{array}{cccc|cccc|cccc|cccc} 1 & 0 & \cdots & 0 & 0 & 0 & \cdots & 0 & 0 & \cdots & 0 & 0 & \cdots & 0 & 0 & \cdots & 0 \\ 0 & 1 & \cdots & 0 & 0 & 0 & \cdots & 0 & 0 & \cdots & 0 & 0 & \cdots & 0 & 0 & \cdots & 0 \\ \vdots & \vdots & \ddots & \vdots & \vdots & \ddots & \vdots & \vdots & \vdots & \ddots & \vdots & \vdots & \ddots & \vdots & \vdots & \ddots & \vdots \\ 0 & 0 & \cdots & 1 & 0 & 0 & \cdots & 0 & 0 & \cdots & 0 & 0 & \cdots & 0 & 0 & \cdots & 0 \\ 0 & 0 & \cdots & 0 & 1 & 0 & \cdots & 0 & 0 & \cdots & 0 & 0 & \cdots & 0 & 0 & \cdots & 0 \\ 0 & 0 & \cdots & 0 & 1 & 0 & \cdots & 1 & 0 & \cdots & 1 & 0 & \cdots & 1 & 0 & \cdots & 1 \end{array} \right), \\ \vec{\mathbf{a}}^T &\equiv \left(a_{0,1} \cdots a_{0,N} \mid a_{1,1} \cdots a_{1,N} \mid a_{2,1} \cdots a_{2,N} \mid a_{3,1} \cdots a_{3,N} \right), \\ \vec{\mathbf{P}}^T &\equiv \left(P_0 \cdots P_N \right). \end{aligned} \quad (2.37)$$

The first order of continuity (eq. (2.34a)) is defined at each of the $N - 1$ interior knots ($l \in (1, N - 1)$). When inserting eq. (2.33) into eq. (2.34a), the left hand side of the equation gives $x = 1$ at the left side of the knot, and the right hand side gives $x = 0$ at the right side. Thus, the first order of

continuity takes the form

$$a_{0,l} + a_{1,l} + a_{2,l} + a_{3,l} - a_{0,l+1} = 0 \quad \forall l \in (1, N-1), \quad (2.38)$$

and can be written in matrix form as $A_0 \vec{a} = \vec{0}$, where

$$A_0 \equiv \left(\begin{array}{cccc|cccc|cccc|cccc} 1 & -1 & 0 & \cdots & 0 & 0 & 1 & 0 & \cdots & 0 & 0 & 1 & 0 & \cdots & 0 & 0 & 1 & 0 & \cdots & 0 & 0 \\ 0 & 1 & -1 & \cdots & 0 & 0 & 0 & 1 & \cdots & 0 & 0 & 0 & 1 & \cdots & 0 & 0 & 0 & 1 & \cdots & 0 & 0 \\ \vdots & \vdots & \vdots & \ddots & \vdots & \vdots & \vdots & \vdots & \ddots & \vdots & \vdots & \vdots & \vdots & \ddots & \vdots & \vdots & \vdots & \vdots & \ddots & \vdots & \vdots \\ 0 & 0 & 0 & \cdots & 1 & -1 & 0 & 0 & \cdots & 1 & 0 & 0 & 0 & \cdots & 1 & 0 & 0 & 0 & \cdots & 1 & 0 \end{array} \right). \quad (2.39)$$

In a similar way, the first order of smoothness (eq. (2.34b)) is

$$a_{1,l} + 2a_{2,l} + 3a_{3,l} - \tilde{r}_l a_{1,l+1} = 0 \quad \forall l \in (1, N-1), \quad (2.40)$$

where the term $\tilde{r}_l \equiv \frac{v_l - v_{l-1}}{v_{l+1} - v_l}$ results from the change of variables in eq. (2.31). This can be written in matrix form as $A_1 \vec{a} = \vec{0}$, where

$$A_1 \equiv \left(\begin{array}{cccc|cccc|cccc|cccc} 0 & \cdots & 0 & 1 & -\tilde{r}_1 & 0 & \cdots & 0 & 0 & 2 & 0 & \cdots & 0 & 0 & 3 & 0 & \cdots & 0 & 0 \\ 0 & \cdots & 0 & 0 & 1 & -\tilde{r}_2 & \cdots & 0 & 0 & 0 & 2 & \cdots & 0 & 0 & 0 & 3 & \cdots & 0 & 0 \\ \vdots & \ddots & \vdots & \vdots & \vdots & \vdots & \ddots & \vdots & \vdots & \vdots & \vdots & \ddots & \vdots & \vdots & \vdots & \ddots & \vdots & \vdots \\ 0 & \cdots & 0 & 0 & 0 & 0 & \cdots & 1 & -\tilde{r}_{N-1} & 0 & 0 & \cdots & 2 & 0 & 0 & 0 & \cdots & 3 & 0 \end{array} \right). \quad (2.41)$$

Lastly, the second order of smoothness (eq. (2.34c)) is

$$a_{2,l} + 3a_{3,l} - \tilde{r}_l^2 a_{2,l+1} = 0 \quad \forall l \in (1, N-1), \quad (2.42)$$

which can be written as $A_2 \vec{a} = \vec{0}$, where

$$A_2 \equiv \left(\begin{array}{cccc|cccc|cccc|cccc} 0 & \cdots & 0 & 0 & \cdots & 0 & 1 & -\tilde{r}_1^2 & 0 & \cdots & 0 & 0 & 3 & 0 & \cdots & 0 & 0 \\ 0 & \cdots & 0 & 0 & \cdots & 0 & 0 & 1 & -\tilde{r}_2^2 & \cdots & 0 & 0 & 0 & 3 & \cdots & 0 & 0 \\ \vdots & \ddots & \vdots & \vdots & \ddots & \vdots & \vdots & \vdots & \ddots & \vdots & \vdots & \vdots & \vdots & \ddots & \vdots & \vdots \\ 0 & \cdots & 0 & 0 & \cdots & 0 & 0 & 0 & 0 & \cdots & 1 & -\tilde{r}_{N-1}^2 & 0 & 0 & \cdots & 3 & 0 \end{array} \right). \quad (2.43)$$

The above constitute a total of $4N - 2$ equations. In order to obtain a closed solution for $w_l(v)$ we need two more equations (constraints). These are obtained by imposing boundary conditions at the two edges of the full v range. Common boundary conditions are parabolic (x^2 , instead of cubic) dependence at the first and last knots, namely $a_{31} = 0$ and $a_{3N} = 0$, or equality of the third derivative in the second and next-to-last knots, namely $a_{3,1} - \tilde{r}_1^3 a_{3,2} = 0$ and $a_{3,N-1} - \tilde{r}_{N-1}^3 a_{3,N} = 0$. These can be written in matrix form as $A_b \vec{a} = \vec{0}$ with

$$A_b^1 \equiv \left(\begin{array}{cccc|cccc|cccc} 0 & \cdots & 0 & 0 & \cdots & 0 & 0 & \cdots & 0 & 1 & 0 & \cdots & 0 & 0 \\ 0 & \cdots & 0 & 0 & \cdots & 0 & 0 & \cdots & 0 & 0 & 0 & \cdots & 0 & 1 \end{array} \right) \quad (2.44)$$

or

$$\mathbf{A}_b^2 \equiv \left(\begin{array}{ccc|ccc} 0 & \cdots & 0 & 0 & \cdots & 0 \\ 0 & \cdots & 0 & 0 & \cdots & 0 \\ 0 & \cdots & 0 & 0 & \cdots & 0 \end{array} \middle| \begin{array}{ccc} 1 & -\tilde{r}_1^3 & 0 \\ 0 & 0 & 0 \\ 0 & 0 & 0 \end{array} \begin{array}{ccc} 0 & 0 & 0 \\ 0 & 1 & -\tilde{r}_{N-1}^3 \end{array} \right), \quad (2.45)$$

respectively.

The entire set of the *above* $4N$ equations can be summarized to

$$\mathbf{A}\vec{a} \equiv \begin{pmatrix} \mathbf{A}_P \\ \mathbf{A}_0 \\ \mathbf{A}_1 \\ \mathbf{A}_2 \\ \mathbf{A}_b \end{pmatrix} \vec{a} = \begin{pmatrix} P_0 \\ \vdots \\ P_n \\ 0 \\ \vdots \\ 0 \end{pmatrix}. \quad (2.46)$$

Now, on the one hand, by definition, $P(v) = \sum_{l=0}^N w_l(v) P_l$. On the other hand, $P(v) = \sum_{i=0}^3 a_{il'} x^i(v) \quad \forall v \in (v_{l'-1}, v_{l'})$. We can compare both terms, to extract $w_l(v)$, through the inversion of eq. (2.46):

$$\begin{aligned} P(v) &= \sum_{i=0}^3 a_{il'} x^i(v) \quad \forall v \in (v_{l'-1}, v_{l'}) \\ &= \sum_{i=0}^3 \sum_{l=0}^N \mathbf{A}_{i \cdot N + l', l}^{-1} P_l x^i(v) \\ &= \sum_{l=0}^N w_l(v) P_l. \end{aligned} \quad (2.47)$$

Therefore, when solving for P_l , the weight functions are:

$$w_l(v) = \sum_{i=0}^3 \mathbf{A}_{i \cdot N + l', l}^{-1} x^i(v) \quad \forall v \in (v_{l'-1}, v_{l'}). \quad (2.48)$$

The event weights $w_{lk} = w_l(v_k)$ are inserted into eq. (2.29), which leads to the derivation of the MLEs and their uncertainties.

One can extend this derivation for a natural spline of higher dimensionality D , while keeping the same number of parameters, by demanding a C^{D-1} continuity at the knots. E.g., for a fifth level spline, one should extend $\mathbf{A}_0, \mathbf{A}_1, \mathbf{A}_2$ and \mathbf{A}_b , and add the corresponding matrices \mathbf{A}_3 and \mathbf{A}_4 to eq. (2.46).

2.4 Comparison of the data to theoretical models and other measurements

It is customary to include theoretical models in plots depicting measured data. Comparing the two is essential for extraction of the underlying physics. When comparing measured data with a

theoretical model, one usually attempts to test the hypothesis that the model describes the data (e.g., by calculating the p -value). In more advanced comparison efforts, one tries to quantify the difference between the model and the measurement, thus deducing to what extent the data exhibits physical effects that are not described by the model.

In this section, we present methods that enable data and calculation comparisons, which utilize the maximum information that is available from the measurements and the associated theoretical model.

2.4.1 Quantifying the difference between measurements and a theoretical model

The common method to compare measurements to a theoretical model is to observe the overall trend of the data as a function of one or more variables, and perform a global comparison to the trend predicted by the model.

We introduce a method that focuses on observing the ratio between the data and a theoretical model prediction for each measured event. This avoids possible loss of information due to inherent assumptions that are included in global trends.

We define the ratio of a measurement to a model as $r_i \equiv P_i^{\text{exp}}/P_i^{\text{calc}}$, where \mathbf{P}^{exp} is the measured polarization in a specific event, and \mathbf{P}^{calc} is the calculated theoretical model value for the kinematics of that specific event. We then calculate the MLEs of \mathbf{r} by maximizing the following log-likelihood function:

$$L(\mathbf{r}) = \sum_{k=1}^n \ln \left(1 + \sum_{i \in \{x,y,z\}} r_i P_{i,k}^{\text{calc}} \lambda_{i,k} \right) \quad (2.49)$$

By redefining $\lambda_{i,k} \rightarrow P_{i,k}^{\text{calc}} \lambda_{i,k}$ the log-likelihood reverts to the form in eq. (2.5), and can be solved for \mathbf{r}_1 according to eq. (2.15).

We can generalize this formalism to varying polarization that depends on a certain variable v , and obtain the MLEs for $\mathbf{r}(v)$, as detailed in section 2.3.

A special case of the above is when the only difference between the measurements and the theoretical model is a scalar factor that is common to all components, $r \equiv P^{\text{exp}}/P^{\text{calc}} = P_x^{\text{exp}}/P_x^{\text{calc}} = P_y^{\text{exp}}/P_y^{\text{calc}} = P_z^{\text{exp}}/P_z^{\text{calc}}$. An example is a polarization transfer measurement to a free proton, as in the $p(\vec{e}, e'\vec{p}')$ reaction, where the proton form factor ratio is well known, and the aim is to extract the analyzing power, the beam polarization, or their product. If this is the case, eq. (2.49) takes the form

$$L(r) = \sum_{k=1}^n \ln \left(1 + r \mathbf{P}_k^{\text{calc}} \cdot \boldsymbol{\lambda}_k \right). \quad (2.50)$$

The MLE of r and its uncertainties can be found by adjusting the definitions of \mathbf{b} , \mathbf{J} , \mathbf{b}' and \mathbf{J}' from eqs. (2.11) and (2.16) respectively:

$$\begin{aligned} b &\equiv \sum_{k=1}^n \mathbf{P}_k^{\text{calc}} \cdot \boldsymbol{\lambda}_k, \\ J &\equiv \sum_{k=1}^n \left(\mathbf{P}_k^{\text{calc}} \cdot \boldsymbol{\lambda}_k \right)^2, \end{aligned}$$

$$\begin{aligned}
b' &\equiv \sum_{k=1}^n \frac{\mathbf{P}_k^{\text{calc}} \cdot \lambda_k}{1 + r \mathbf{P}_k^{\text{calc}} \cdot \lambda_k}, \\
J' &\equiv \sum_{k=1}^n \left(\frac{\mathbf{P}_k^{\text{calc}} \cdot \lambda_k}{1 + r \mathbf{P}_k^{\text{calc}} \cdot \lambda_k} \right)^2.
\end{aligned} \tag{2.51}$$

The algebra of eqs. (2.13), (2.15) and (2.9) still holds:

$$\begin{aligned}
r_0 &= J^{-1} b, \\
r_1 &= r_0 + [J'^{-1} b']_{r=r_0}, \\
\sigma_{r_1} &= J'|_{r=r_1}^{-1/2}.
\end{aligned} \tag{2.52}$$

Notice that in this special case, even if r is not expected to depend on any kinematical variable, it could vary with time (t), and thus be different for each event. In order to take such temporal variations into account, one can generalize eqs. (2.50–2.52) to r that depends on a single variable (time in this case) according to section 2.3, and deduce $r(t)$.

2.4.2 Tests of statistical consistency between measurements and calculations (p -value)

We define L_{H_1} to be the log-likelihood function of the experimental data, whose maximum is given by the MLEs $r_{i,1} \forall i \in \{x, y, z\}$, and L_{H_0} to be the log-likelihood function of the theoretical model, whose MLEs are $r_i = 1 \forall i \in \{x, y, z\}$, by definition. The ‘null hypothesis’ (H_0), which is the hypothesis that the experimental data and the theoretical model are consistent, is tested by using the ratio of these two likelihoods, or the difference of the two log-likelihoods, $\Lambda \equiv L_{H_1} - L_{H_0} = L(\mathbf{r}_1) - L(\mathbf{1})$, where $L(\mathbf{r})$ is given in eq. (2.49).

According to Wilks’ theorem for log-likelihood ratio statistics, for a large number of events, 2Λ has a χ^2 distribution with ν degrees of freedom, where ν is the difference between the numbers of parameters in the compared models [6, 11]. In this case, one ‘model’, the experimental data, has 3 parameters ($r_{i,1}$), and the theoretical model (the ‘null model’) has no parameters (since $r_i = 1$) so $\nu = 3$. The ‘null hypothesis’ test is performed by calculating the cumulative distribution function (CDF) of the distribution, $p \equiv p(\chi^2, \nu) = p(2\Lambda, 3)$. If $p > 5\%$, we cannot reject the ‘null hypothesis’, namely, the experiment and model are consistent [6].

The above process can be generalized to varying polarization. If $\mathbf{r} = \mathbf{r}(\nu)$ and the ν range is divided into N bins, then the number of degrees of freedom changes to $\nu = 3(N + 1)$, and other than that there is no change.

A more sophisticated test of the validity of the model is to check consistency up to a normalization factor for the polarization-transfer, r , which might arise from, e.g., a systematic error in the beam polarization. The likelihood-ratio log is $\Lambda = L(\mathbf{r}_1) - L(r_1)$, where $L(\mathbf{r})$ and $L(r)$ are given by eqs. (2.49–2.50), respectively. Since the theoretical model has now one parameter, the difference in degrees of freedom is 2, and the ‘null hypothesis’ test is $p(2\Lambda, 2) > 5\%$.

Also here, a varying $\mathbf{r}(\nu)$ with N bins will increase the number of degrees of freedom to $2(N + 1)$.

2.4.3 Plotting model predictions with data

When depicting experimental data, it is common to plot a model's prediction with it. However, while the measurement result (\mathbf{P}^{exp}) is calculated for an ensemble of events, the model (\mathbf{P}^{calc}) is calculated for each event separately.

The traditional way to present the model is to take its average over the events that constitute the experimental sample, $\mathbf{P}_a^{\text{calc}} \equiv n^{-1} \sum_{k=1}^n \mathbf{P}_k^{\text{calc}}$. However, one can perform a better comparison by using a weighted average of the model dictated by the experimental sample. As will be evident from the derivation below, this weight turns out to be the effective analyzing power of the event. The experimental events are weighted by the analyzing power, and now the theoretical ones are weighted in the same manner.

When observing a plot with data points and the respective model predictions, the quarry is the difference between the two: $\boldsymbol{\delta} \equiv \mathbf{P}^{\text{exp}} - \mathbf{P}^{\text{calc}}$. To estimate $\boldsymbol{\delta}$ we calculate the log-likelihood:

$$L(\boldsymbol{\delta}) = \sum_{k=1}^n \ln \left(1 + \left(\boldsymbol{\delta} + \mathbf{P}_k^{\text{calc}} \right) \cdot \lambda_k \right). \quad (2.53)$$

Taking the linear approximation of section 2.1.2, we obtain

$$L(\boldsymbol{\delta}) \simeq \sum_{k=1}^n \left[\left(\boldsymbol{\delta} + \mathbf{P}_k^{\text{calc}} \right) \cdot \lambda_k - \frac{1}{2} \left(\left(\boldsymbol{\delta} + \mathbf{P}_k^{\text{calc}} \right) \cdot \lambda_k \right)^2 \right], \quad (2.54)$$

and using the definitions of eq. (2.11), this expression is reduced to

$$L(\boldsymbol{\delta}) \simeq \boldsymbol{\delta} \cdot \mathbf{b} + C_1 - \boldsymbol{\delta}^T \mathbf{J} \boldsymbol{\delta} / 2 - \boldsymbol{\delta}^T \mathbf{J} \mathbf{P}_w^{\text{calc}} - C_2, \quad (2.55)$$

where C_1 and C_2 are constants that are independent of $\boldsymbol{\delta}$, and

$$\mathbf{P}_w^{\text{calc}} \equiv \mathbf{J}^{-1} \sum_{k=1}^n \left(\left(\mathbf{P}_k^{\text{calc}} \cdot \lambda_k \right) \lambda_k \right). \quad (2.56)$$

Comparing this to eq. (2.3), one indeed sees that $\mathbf{P}_w^{\text{calc}}$ is weighted by an effective analyzing power, as described above.

The linear log-likelihood is maximized at

$$\boldsymbol{\delta}_0 = \mathbf{J}^{-1} \left(\mathbf{b} - \mathbf{J} \mathbf{P}_w^{\text{calc}} \right) = \mathbf{P}_0 - \mathbf{P}_w^{\text{calc}}. \quad (2.57)$$

The definition of $\mathbf{P}_w^{\text{calc}}$ can be extended to a continuous description of the data by redefining $\lambda_{i,k} \rightarrow w_{Ik} \lambda_{i,k}$, where w_{Ik} were defined in section 2.3.

2.4.4 Comparisons between measured results from two experiments

In addition to comparing experimental data to theoretical calculations, there is interest in comparing two experimental data sets, to determine if they are consistent. For example, one could be interested in comparing polarization transfer to two different target nuclei. In such a comparison, one needs to account for overall differences between the data sets, for example, beam polarization.

We would like to test whether two data sets (A and B) describe the same polarization-transfer, i.e., if they differ from each other by a scalar factor $r \equiv P^B/P^A = P_x^B/P_x^A = P_y^B/P_y^A = P_z^B/P_z^A$ that incorporates the possible differences in the measurement conditions. Following 2.4.2, the likelihood-ratio log is $\Lambda = L(\mathbf{P}_A, \mathbf{P}_B) - L(r, \mathbf{P})$, where

$$L(\mathbf{P}_A, \mathbf{P}_B) = \sum_{k=1}^{n_A} \ln(1 + \mathbf{P}_A \cdot \boldsymbol{\lambda}_k) + \sum_{k=1}^{n_B} \ln(1 + \mathbf{P}_B \cdot \boldsymbol{\lambda}_k), \quad (2.58)$$

and

$$L(r, \mathbf{P}) = \sum_{k=1}^{n_A} \ln(1 + \mathbf{P} \cdot \boldsymbol{\lambda}_k) + \sum_{k=1}^{n_B} \ln(1 + r\mathbf{P} \cdot \boldsymbol{\lambda}_k). \quad (2.59)$$

$L(\mathbf{P}_{1,A}, \mathbf{P}_{1,B})$ can be estimated easily by summing the log-likelihood for each data set at its maximum, according to eq. (2.15). However, the approximation of section 2.1.2 for $L(r, \mathbf{P})$, yields a non-linear set of equations for the maximum:

$$L(r, \mathbf{P}) \simeq \mathbf{P} \cdot (\mathbf{b}_A + r\mathbf{b}_B) - (\mathbf{P}\mathbf{J}_A\mathbf{P} + r^2\mathbf{P}\mathbf{J}_B\mathbf{P})/2, \quad (2.60)$$

$$\partial_r L \simeq \mathbf{P} \cdot \mathbf{b}_B - r\mathbf{P}\mathbf{J}_B\mathbf{P} = 0, \quad (2.61)$$

$$\nabla_{\mathbf{P}} L \simeq \mathbf{b}_A + r\mathbf{b}_B - (\mathbf{J}_A + r^2\mathbf{J}_B)\mathbf{P} = \mathbf{0}. \quad (2.62)$$

Searching for a 4-dimensional (P_x, P_y, P_z, r) optimization is CPU intensive. However, we can reduce the problem to a 1-dimensional numerical optimization that requires a single loop over the sample, by noting the log-likelihood ridge at

$$\mathbf{P}_0(r) = (\mathbf{J}_A + r^2\mathbf{J}_B)^{-1} (\mathbf{b}_A + r\mathbf{b}_B), \quad (2.63)$$

and recalling that $\mathbf{b}_A, \mathbf{b}_B, \mathbf{J}_A$ and \mathbf{J}_B are available from the maximization of $L(\mathbf{P}_A, \mathbf{P}_B)$, leaving a dependence only on r .

We maximize the likelihood by starting from $r_0 = P_{1,B}/P_{1,A}$, and taking Newton–Raphson steps,

$$r_{i+1} = r_i - \left[\frac{dL}{dr} / \frac{d^2L}{dr^2} \right]_{\mathbf{P}=\mathbf{P}_0(r_i)}^{r=r_i}, \quad (2.64)$$

where

$$\frac{dL}{dr} = \partial_r L + \nabla_{\mathbf{P}} L \cdot \partial_r \mathbf{P} \simeq \mathbf{P} \cdot \mathbf{b}_B - r\mathbf{P}\mathbf{J}_B\mathbf{P}, \quad (2.65)$$

and

$$\begin{aligned} \frac{d^2L}{dr^2} &\simeq \partial_r^2 L + \nabla_{\mathbf{P}} \partial_r L \cdot \partial_r \mathbf{P} \\ &= -r\mathbf{P}\mathbf{J}_B\mathbf{P} + (\mathbf{b}_B - r\mathbf{J}_B\mathbf{P}) \cdot \left((\mathbf{J}_A + r^2\mathbf{J}_B)^{-1} \mathbf{b}_B - 2r \frac{\mathbf{J}_A^{-1}\mathbf{J}_B\mathbf{J}_A^{-1} (\mathbf{b}_A + r\mathbf{b}_B)}{(1 + r^2 \text{trace}(\mathbf{J}_A^{-1}\mathbf{J}_B))^2} \right). \end{aligned} \quad (2.66)$$

As before, the approximations in eqs. (2.65–2.66) are those of section 2.1.2.

We define (r_1, \mathbf{P}_1) as the maximum of the ridge as. The exact gradient of the log-likelihood is

$$\begin{aligned}\partial_r L &= \sum_{k=1}^{n_B} \frac{\mathbf{P} \cdot \boldsymbol{\lambda}_k}{1 + r \mathbf{P} \cdot \boldsymbol{\lambda}_k}, \\ \nabla_{\mathbf{P}} L &= \sum_{k=1}^{n_A} \frac{\boldsymbol{\lambda}_k}{1 + \mathbf{P} \cdot \boldsymbol{\lambda}_k} + r \sum_{k=1}^{n_B} \frac{\boldsymbol{\lambda}_k}{1 + r \mathbf{P} \cdot \boldsymbol{\lambda}_k},\end{aligned}\quad (2.67)$$

and the Hessian is

$$H = - \sum_{k=1}^{n_A} \frac{\begin{pmatrix} 0 & \mathbf{0}^T \\ \mathbf{0} & \boldsymbol{\lambda}_k \otimes \boldsymbol{\lambda}_k \end{pmatrix}}{(1 + \mathbf{P} \cdot \boldsymbol{\lambda}_k)^2} - \sum_{k=1}^{n_B} \frac{\begin{pmatrix} (\mathbf{P} \cdot \boldsymbol{\lambda}_k)^2 & r \mathbf{P} \cdot \boldsymbol{\lambda}_k \otimes \boldsymbol{\lambda}_k \\ r \mathbf{P} \cdot \boldsymbol{\lambda}_k \otimes \boldsymbol{\lambda}_k & r^2 \boldsymbol{\lambda}_k \otimes \boldsymbol{\lambda}_k \end{pmatrix}}{(1 + r \mathbf{P} \cdot \boldsymbol{\lambda}_k)^2} + \sum_{k=1}^{n_B} \frac{\begin{pmatrix} 0 & \boldsymbol{\lambda}_k^T \\ \boldsymbol{\lambda}_k & 0_{3 \times 3} \end{pmatrix}}{1 + r \mathbf{P} \cdot \boldsymbol{\lambda}_k}.\quad (2.68)$$

Finally, the exact maximum is sought through $\begin{pmatrix} r_{i+1} \\ \mathbf{P}_{i+1} \end{pmatrix} = \begin{pmatrix} r_i \\ \mathbf{P}_i \end{pmatrix} - \left[H^{-1} \left(\frac{\partial_r L}{\nabla_{\mathbf{P}} L} \right) \right]_{\begin{pmatrix} r_i \\ \mathbf{P}_i \end{pmatrix}}$, and the ‘null hypothesis’ test is $p(2\Lambda, 2) > 5\%$.

This derivation can be extended for maximizing $L(r, \mathbf{P}(v))$ and $L(r(v), \mathbf{P}(v))$.

2.5 Combining the method’s tools

In section 2.2 we showed how to extract the components of a constant polarization in spherical coordinates, independent of any model. In section 2.3 we showed how to extract a varying polarization in Cartesian coordinates, again, independent of any model. In section 2.4 we showed how to compare a measurement with a model in Cartesian coordinates, and proclaim that it could be extended to a varying description.

In appendix A, we demonstrate how these three tools are combined to a continuous description of the ratio between a measurement and its corresponding calculated prediction, in spherical coordinates. Further, we provide in appendix A the full algorithm, which can be implemented in a computer program.

3 Validity and advantages of the method

In order to demonstrate the validity and advantages of this method, we apply it to analyze simulated polarization-transfer data sets. We produced two types of simulated events:

1. Events with a constant polarization, which we analyzed according to the procedures of section 2.1.2 and section 2.2.
2. Events with polarization that depends on a kinematical parameter, to demonstrate the continuous presentation discussed in section 2.3 and the modeling tools in section 2.4.

Thus, we test the usefulness of the MLEs, and demonstrate the advantages of the maximization process and the presentation in spherical of coordinates.

3.1 Simulation of a constant polarization

In the first test we applied the new analysis method to simulated data with a constant polarization to verify how well we reproduce the ‘input’ polarization and to estimate the inherent error of this method.

3.1.1 Generation of simulated events

We simulated 50,000 polarization-transfer experiments, where each experiment consists of 100,000 events. The polarization was set to be the same for all events in all the simulated experiments: $\mathbf{P}_{\text{input}} = (-0.5, 0, 0.5)$. The polarization of each event was multiplied by a constant analyzing power of 0.25 in all the simulated experiments. The spin vector of each event was rotated by a randomly generated spin precession matrix (\mathbf{S}) transforming the spin from target to a hypothetical polarimeter (see figure 1a), where the three Euler angles’ distributions are

$$\begin{aligned}\alpha_{\text{Euler}} &\sim \mathcal{N}(180^\circ, 15^\circ) \\ \beta_{\text{Euler}} &\sim \mathcal{N}(322^\circ, 15^\circ) \\ \gamma_{\text{Euler}} &\sim \mathcal{N}(90^\circ, 15^\circ).\end{aligned}\tag{3.1}$$

Such distributions are typical to some experiments using small solid angle spectrometers [1, 8–10, 12–16]. The scattering by the carbon analyzer was simulated by assigning each event an azimuthal angle ϕ_{FPP} from a sinusoidal distribution (eq. (2.2)).

For each one of the 50,000 simulated experiments, we extracted \mathbf{P}_{exp} and $\Delta\mathbf{P}_{\text{exp}}$, by applying the new procedure and analyzing the 100,000 transformed events (according to sections 2.1.2 and 2.2). We define the error of each experiment as $\mathbf{P}_{\text{error}} \equiv \mathbf{P}_{\text{exp}} - \mathbf{P}_{\text{input}}$. Notice that this error describes exactly the error of the procedure, since neither the input events nor any of the simulated transformations have any inherent errors and no errors in the measurements of the angles or positions are assumed or applied (unlike a real simulation of an experimental detector).

To study our method’s validity, we investigated the distributions of $\mathbf{P}_{\text{error}}$ and of the uncertainties $\Delta\mathbf{P}_{\text{exp}}$ obtained for each data set.

3.1.2 Results of the method applied to simulated events with constant polarization

The distributions of P_i^{error} ($i \in \{x, y, z\}$) for the 50,000 simulated experiments are shown in figure 2. The mean value of each distribution $\langle P_i^{\text{error}} \rangle$ is consistent with zero, as are the skewness and excess kurtosis of each distribution. These results confirm that the MLEs for (P_x, P_y, P_z) obtained by this analysis method are normally distributed and not biased.

The distributions of the uncertainties ΔP_i^{exp} ($i \in \{x, y, z\}$) obtained from each data set, are shown in figure 3. The calculated means, $\langle \Delta P_i^{\text{exp}} \rangle$, are consistent with the standard deviations of the extracted polarization, $\sigma [P_i^{\text{exp}}]$. This consistency indicates that the estimated uncertainties ΔP_i^{exp} are also unbiased in this method.

To assess the reliability of the relative uncertainties obtained from the analysis, we compared the width of the error distribution to that of the P_i^{exp} distribution by $\sigma [\Delta P_i^{\text{exp}}] / \sigma [P_i^{\text{exp}}]$. The resultant estimated uncertainty on the calculated uncertainties is $\sim 0.2\%$ (see figure 3).

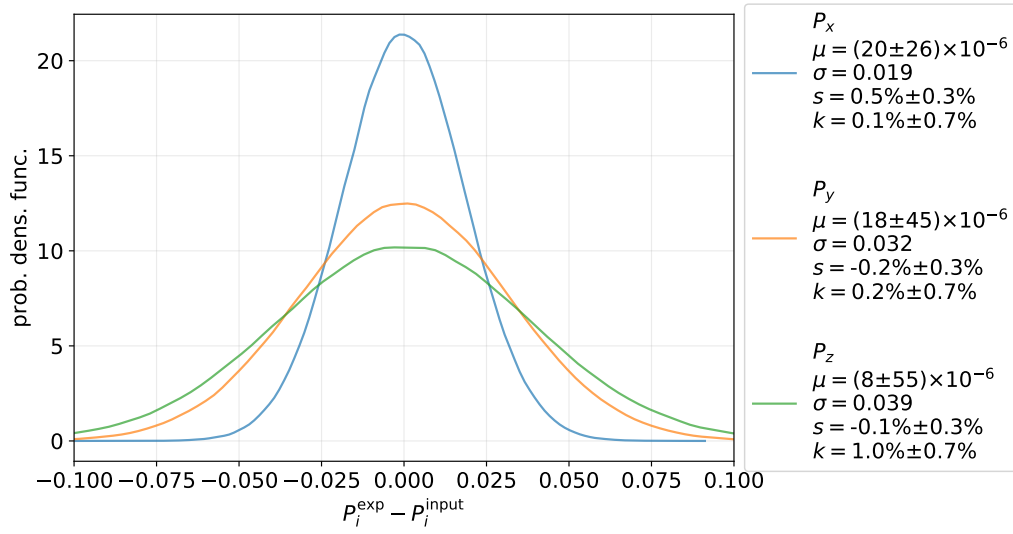


Figure 2: The distribution of the simulated polarization component estimation errors: $P_i^{\text{error}} \equiv P_i^{\text{exp}} - P_i^{\text{input}}$ for $i \in \{x, y, z\}$. The legend shows the mean (μ), standard deviation (σ), skewness (s) and excess kurtosis (k) for each distribution.

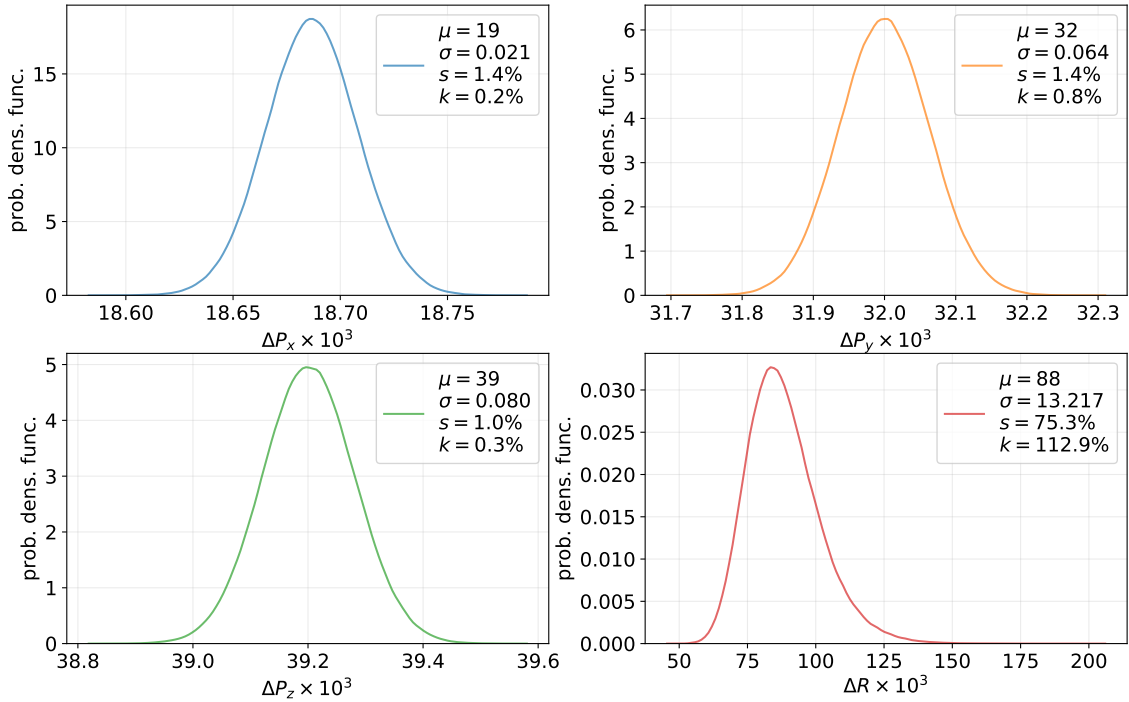


Figure 3: The distribution of the simulated polarization component uncertainty estimators. The legend shows the mean (μ), standard deviation (σ), skewness (s) and excess kurtosis (k) for each distribution.

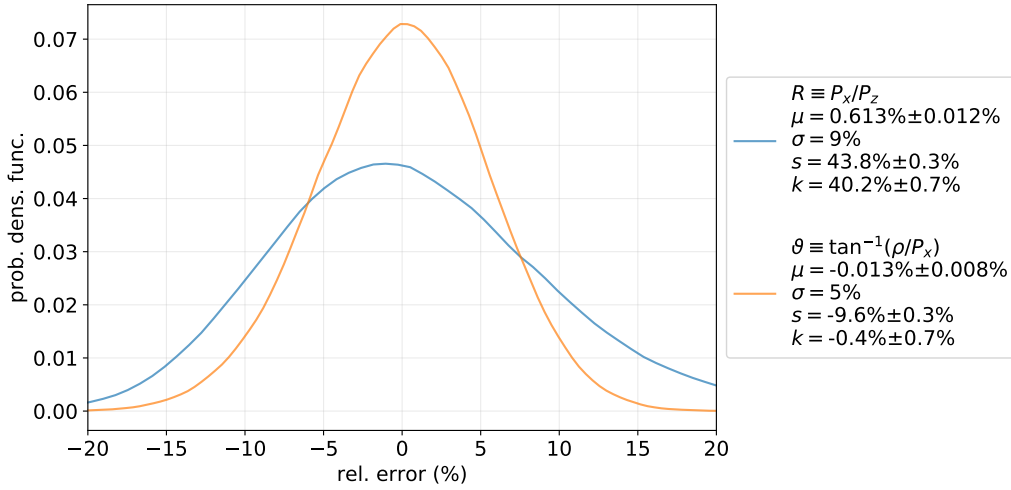


Figure 4: The distribution of the simulated polarization estimation relative errors for R and ϑ : $(R_{\text{exp}} - R_{\text{input}}) / R_{\text{input}}$ and $(\vartheta_{\text{exp}} - \vartheta_{\text{input}}) / \vartheta_{\text{input}}$. The legend shows the mean (μ), standard deviation (σ), skewness (s) and excess kurtosis (k) for each distribution.

While the determination of the individual components is obtained with relatively small uncertainties as expected from the statistics, the determination of component ratios results in large uncertainties, which is typical to analyses using the standard method. This may be an important issue in polarization experiments where beam or target polarization are measured with relatively large uncertainties, which in turn introduce large systematic errors on polarization components. Determination of the component ratio such as P_x/P_z largely cancels this uncertainty and is used routinely to determine the electric to magnetic form factors ratio. Thus we conclude with examining this quantity in comparison to alternative ratios obtained when using spherical coordinates.

The distribution of $R = \frac{P_x}{P_z}$ in the 50,000 experiments shows that the estimator is biased ($\langle R_{\text{exp}} - R_{\text{input}} \rangle$ is inconsistent with zero), and has significantly large skewness and excess kurtosis (see figure 4). This should be expected, since for a bi-normal set (x, y) , $E \left[\left| \frac{x}{y} \right| \right] > \frac{E[|x|]}{E[|y|]}$. When extracting the propagated uncertainty of R from the separate polarization components,

$$\Delta R \equiv R \sqrt{\Delta P_x^2 / P_x^2 + \Delta P_z^2 / P_z^2 - 2 \text{Cov}[P_x, P_z] / P_x P_z}$$

(eq. (2.18)), it is found to be unbiased. However, the relative uncertainty of the estimated uncertainty for R , estimated by evaluating $\sigma[\Delta R] / \sigma[R]$, was found to be $\sim 15\%$, i.e. 100 times larger than those of the separate components (see figure 3).

Unlike R , when using spherical coordinates (section 2.2) the MLE for ϑ (which comprises a similar physical meaning to R , especially when $P_y = 0$, see section 2.2.1) is unbiased and almost normal (see figure 4). The relative uncertainty of the estimated uncertainty for ϑ , estimated by $\sigma[\Delta \vartheta] / \sigma[\vartheta]$, is $\sim 2\%$, much narrower than that of R . This better result is due to avoiding propagation, as discussed in section 2.2.

In addition to generating narrower and more reliable uncertainties, the simulation demonstrated the efficiency of our method regarding CPU usage. In standard methods such as Minuit or Simplex,

the typical number of numerical steps is ~ 10 , and the likelihood function is calculated between 60 and 100 times [12]. This process can not be parallelized. In contrast, our method required only a single Newton–Raphson step to achieve convergence in each of the 50,000 experiments. Therefore, our method requires approximately 100 times less CPU time with respect to standard methods.

3.2 Simulation of events with varying polarization

We turn to demonstrate the advantage of the continuous presentation of polarization that depends on a certain parameter. For this purpose we produced events with a polarization that depends on a kinematical variable, and analyzed them according to the procedures of sections 2.3 and 2.4. Thus, we survey the usefulness of a cubic spline description.

3.2.1 Simulation and results

For simplicity, we analyze a simulated data set whose polarization depends on a single parameter. This was done by assuming that in the simulated experiment a proton’s polarization is known but the measured polarization is scaled by the ‘system’ analyzing power which depends on the proton momentum. Thus the measurement should yield the momentum dependence of the analyzing power.

We simulated one polarization measurement experiment of 300,000 events. The polarization was set to be the same for all events: $\mathbf{P}_{\text{input}} = (-0.4, 0.1, 0.6)$. For each event the proton was assigned a kinetic energy (T_p) generated from a normal distribution. The polarization of each event was multiplied by an analyzing power (a_y) that depends on T_p . As in the previous section, the spin vector of each event was rotated by a randomly generated spin precession matrix (\mathbf{S}) transforming the spin from the target to the polarimeter, where the three Euler angles’ distributions are given in eq. (3.1). The scattering of each event by the polarimeter analyzer was simulated by assigning each event an azimuthal angle ϕ_{FPP} from a sinusoidal distribution (eq. (2.2)). Further details can be found in the [simulation documentation](#).

We analyzed the data in the “traditional way”, in bins of kinetic energy (section 2.3.1). The analysis yields the ratio of the measured polarization components to those of the constant polarization considered event by event and averaged over each bin. It represents the average analyzing power over the bin. The analysis was repeated using a cubic spline representation of the T_p dependence of the measured a_y , applying the MLE approach according to section 2.3.3.

In figure 5 we compare the results of both methods. We note that the spline result shows the full structure of the input function, and does not exhibit any false structure. This cannot be stated about the binned results where one may be tempted to associate statistical fluctuations with some extra structure, as suggested by the fit in figure 5. One may be concerned that addition of more parameters to the spline will cause false structure to emerge due to over-fitting. However, using Wilks’ theorem for the likelihood-ratio, one can show that extra parameters are redundant as discussed in section 2.4 and the [simulation documentation](#). We also note that the continuous presentation results in an uncertainty band which is much narrower than the uncertainties in the binned analysis (where each bin is independent of its neighbors) particularly in the bins with the low statistics.

We can use the same simulation to show that if in the above problem the analyzing power is known up to a unknown factor, we can reduce the uncertainty of the estimated factor by $\sim 15\%$ by using the method of section 2.4.1.

3.2.2 Documented source code notebook

The detailed simulation description accompanied with source code snippets is [available on-line](#).

The source code “Jupyter” notebook can be downloaded from [here](#) (file size = 300 kB, run time ≈ 5 seconds).

The notebook contains the implementation of the majority of the formulæ from section §2.

4 Summary and Conclusions

We introduced a new method to analyze polarization measurement data. The analysis is performed using spherical coordinates and a continuous presentation of the measurements. The spherical coordinates (P , ρ and ϑ) are unaffected by mixing of the P_z and P_y components which in turn affects the uncertainty in the measurements of the components ratio. Using ϑ instead of R does not change the physical interpretation. However, if one needs an observable that is only a function of R , we can redefine eq. (2.19) so that $\tan \vartheta \equiv P_x/P_z$ without changing the formalism.

The continuous presentation (rather than dividing the measured range into arbitrary bins in which discrete average values are determined, independent of each other) results in an uncertainty band which is narrower than the errors in a binned analysis, particularly when some bins are measured with lower statistics. It also allows a reliable comparison of the measurement to other measurements or calculations. The new method yields even smaller uncertainties which in the

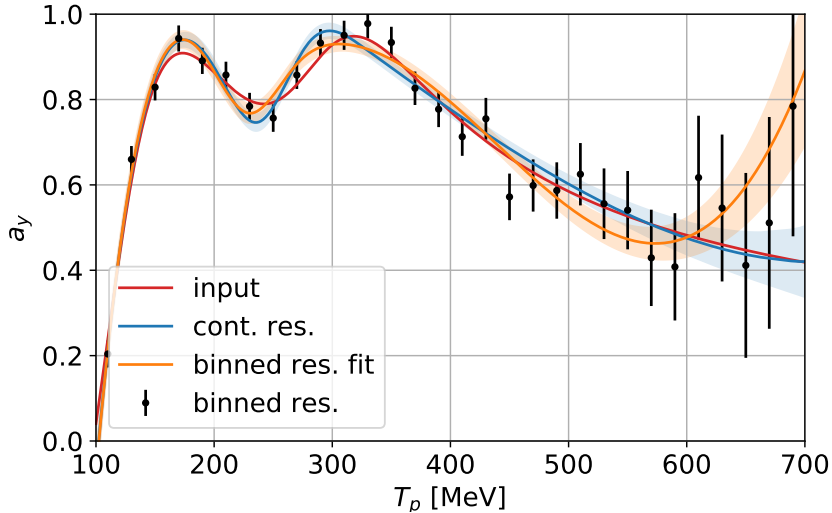


Figure 5: Simulated analyzing power. We compare the input form (red line), with binned (black error-bars) and continuous (blue band) analyses. For a full comparison, we fitted the binned results to a cubic spline with the same number of parameters as the continuous description (orange band). See the [simulation documentation](#) for additional details and fits.

simulated examples were reduced by about 20% (see figure 5). When the data are described by well known models or parameterizations (like a dipole form factor) the uncertainty can be reduced even further (see section 2.4).

Our new method is more efficient in CPU by about two orders of magnitude, when compared with conventional methods currently in use.

Acknowledgments

The authors would like to thank Dr. Linda Montag for her help in the manuscript preparation.

This work is supported by the Israel Science Foundation (Grant 390/15) of the Israel Academy of Arts and Sciences, by the Israel Atomic Energy Commission (the PAZI Foundation), and by the Israel Ministry of Science, Technology and Space.

Appendix

A Full Example

As discussed in section 2.5, in section 2.2 we use spherical coordinates for the simplest case. In section 2.3 we deal with varying polarization only in Cartesian coordinates, and in section 2.4 we compare a measurement with a model only in Cartesian coordinates.

Here we demonstrate how these three tools are combined to a continuous description of the ratio between a measurement and its corresponding calculated prediction, in spherical coordinates. Further, we provide the full algorithm, which can be implemented in a computer program.

A.1 Derivation

We measure the polarization-transfer in the ${}^2\text{H}(\vec{e}, e'\vec{p})n$ reaction at a fixed beam energy, as a function of the missing momentum p_m . We would like to account for the finite acceptance in Q^2 , θ_{pq} and ϕ_{pq} , while comparing with a model that predicts that $P_y = 0$ (and therefore $\varphi_{\text{mod}} = 0$).

We divide the p_m range to N segments with 3 $(N + 1)$ parameters according to section 2.3.3.

Here we take the short hand notation of $w_l = w_l(p_m)$, and define $r(p_m) \equiv P_{\text{exp}}(p_m)/P_{\text{calc}}(p_m)$, $\delta(p_m) \equiv \vartheta_{\text{exp}}(p_m) - \vartheta_{\text{calc}}(p_m)$. Since $\varphi_{\text{calc}} = 0$, we will use $\varphi \equiv \varphi_{\text{exp}}$.

γ is:

$$\begin{aligned}
 \gamma &= P_{\text{exp}}(\lambda_x \cos \vartheta_{\text{exp}} + \sin \vartheta_{\text{exp}}(\lambda_y \sin \varphi + \lambda_z \cos \varphi)) \\
 &= r P_{\text{calc}}(\lambda_x \cos(\vartheta_{\text{calc}} + \delta) + \sin(\vartheta_{\text{mod}} + \delta)(\lambda_y \sin \varphi + \lambda_z \cos \varphi)) \\
 &= \left(\sum_{l=0}^N w_l r_l \right) P_{\text{calc}} \times \\
 &\quad \times \left(\lambda_x \cos \left(\vartheta_{\text{calc}} + \sum_{l=0}^N w_l \delta_l \right) + \sin \left(\vartheta_{\text{calc}} + \sum_{l=0}^N w_l \delta_l \right) \times \right. \\
 &\quad \left. \times \left(\lambda_y \sin \sum_{l=0}^N w_l \varphi_l + \lambda_z \cos \sum_{l=0}^N w_l \varphi_l \right) \right) \tag{A.1}
 \end{aligned}$$

The the first derivatives of γ are:

$$\begin{aligned}
 \partial_{r_l} \gamma &= \frac{w_l \gamma}{\sum_{l'} w_{l'} r_{l'}} \equiv w_l \lambda'_r \\
 \partial_{\delta_l} \gamma &= w_l (\tau \xi - \lambda_x \rho) \equiv w_l \lambda'_\delta \\
 \partial_{\varphi_l} \gamma &= w_l \bar{\xi} \equiv w_l \lambda'_\varphi, \tag{A.2}
 \end{aligned}$$

where τ , ξ , $\bar{\xi}$ and ρ are all functions of p_m and are model dependent (as specified in eq. (A.4) below). The second derivatives of γ are:

$$\begin{aligned}
 \partial_{r_l} \partial_{r_{l'}} \gamma &= 0 \\
 \partial_{\delta_l} \partial_{\delta_{l'}} \gamma &= -w_l w_{l'} \gamma \equiv -w_l w_{l'} \lambda'_{\delta\delta} \\
 \partial_{\varphi_l} \partial_{\varphi_{l'}} \gamma &= -w_l w_{l'} \bar{\xi} \equiv -w_l w_{l'} \lambda'_{\varphi\varphi}
 \end{aligned}$$

$$\begin{aligned}
\partial_{r_l} \partial_{\delta_{l'}} \gamma &= \frac{w_l w_{l'}}{\sum_{l''} w_{l''} r_{l''}} (\tau \xi - \lambda_x \rho) \equiv -w_l w_{l'} \lambda'_{r\delta} \\
\partial_{r_l} \partial_{\varphi_{l'}} \gamma &= \frac{w_l w_{l'}}{\sum_{l''} w_{l''} r_{l''}} \bar{\xi} \equiv -w_l w_{l'} \lambda'_{r\varphi} \\
\partial_{\delta_l} \partial_{\varphi_{l'}} \gamma &= w_l w_{l'} \tau \bar{\xi} \equiv -w_l w_{l'} \lambda'_{\delta\varphi}.
\end{aligned} \tag{A.3}$$

A.2 Algorithm

1. We divide the events to N bins, and calculate the cubic spline weights according to eq. (2.48).
2. We start from $r_l = 1$, $\delta_l = \varphi_l = 0$.
3. For each event we

(a) calculate

$$\begin{aligned}
\sum_w r &\equiv \sum_{l=0}^N w_l r_l, \\
\rho &= P_{\text{calc}} \sin \left(\vartheta_{\text{calc}} + \sum_{l=0}^N w_l \delta_l \right) \sum_w r, \\
\xi &= \rho \left(\lambda_y \sin \sum_{l=0}^N w_l \varphi_l + \lambda_z \cos \sum_{l=0}^N w_l \varphi_l \right), \\
\bar{\xi} &= \rho \left(\lambda_y \cos \sum_{l=0}^N w_l \varphi_l - \lambda_z \sin \sum_{l=0}^N w_l \varphi_l \right), \\
\tau &= \cot \left(\vartheta_{\text{calc}} + \sum_{l=0}^N w_l \delta_l \right), \\
\gamma &= \xi + \lambda_x P_{\text{calc}} \cos \left(\vartheta_{\text{calc}} + \sum_{l=0}^N w_l \delta_l \right) \sum_w r,
\end{aligned} \tag{A.4}$$

(b) followed by

$$\begin{pmatrix} \lambda'_{rk} \\ \lambda'_{\delta k} \\ \lambda'_{\varphi k} \end{pmatrix} = \begin{pmatrix} \gamma / \sum_w r \\ \tau \xi - \lambda_x \rho \\ \bar{\xi} \end{pmatrix}, \tag{A.5}$$

and

$$\begin{pmatrix} \lambda'_{r\delta k} \\ \lambda'_{\delta\delta k} \\ \lambda'_{\delta\varphi k} \\ \lambda'_{r\varphi k} \\ \lambda'_{\varphi\varphi k} \end{pmatrix} = \begin{pmatrix} (\lambda_x \rho - \tau \xi) / \sum_w r \\ \gamma \\ -\tau \bar{\xi} \\ -\bar{\xi} / \sum_w r \\ \xi \end{pmatrix}, \tag{A.6}$$

(c) which are then multiplied for each l for $\frac{w_{lk}}{1+\gamma_k} \begin{pmatrix} \lambda'_{rk} \\ \lambda'_{\delta k} \\ \lambda'_{\varphi k} \end{pmatrix}$,

(d) which is outer-squared for $\frac{w_{lk}w_{l'k}}{(1+\gamma_k)^2} \begin{pmatrix} \lambda_{rk}^2 & \lambda'_{rk}\lambda'_{\delta k} & \lambda'_{rk}\lambda'_{\varphi k} \\ \lambda'_{rk}\lambda'_{\delta k} & \lambda_{\delta k}^2 & \lambda'_{\delta k}\lambda'_{\varphi k} \\ \lambda'_{rk}\lambda'_{\varphi k} & \lambda'_{\delta k}\lambda'_{\varphi k} & \lambda_{\varphi k}^2 \end{pmatrix},$

(e) and finally for each ll' pair we produce $\frac{w_{lk}w_{l'k}}{1+\gamma_k} \begin{pmatrix} 0 & \lambda'_{r\delta k} & \lambda'_{r\varphi k} \\ \lambda'_{r\delta k} & \lambda'_{\delta\delta k} & \lambda'_{\delta\varphi k} \\ \lambda'_{r\varphi k} & \lambda'_{\delta\varphi k} & \lambda'_{\varphi\varphi k} \end{pmatrix}.$

4. We take a Newton–Raphson step by by:

(a) summing for the sub-vectors $\bar{\mathbf{b}}_l''$ and sub-matrices $\bar{\mathbf{J}}_{ll}''$, according to

$$\bar{\mathbf{b}}_l'' = \sum_{k=1}^n \frac{w_{lk}}{1+\gamma_k} \begin{pmatrix} \lambda'_{rk} \\ \lambda'_{\delta k} \\ \lambda'_{\varphi k} \end{pmatrix}, \quad (\text{A.7})$$

and

$$\bar{\mathbf{J}}_{ll}'' = \sum_{k=1}^n \frac{w_{lk}w_{l'k}}{(1+\gamma_k)^2} \begin{pmatrix} \lambda_{rk}^2 & \lambda'_{rk}\lambda'_{\delta k} & \lambda'_{rk}\lambda'_{\varphi k} \\ \lambda'_{rk}\lambda'_{\delta k} & \lambda_{\delta k}^2 & \lambda'_{\delta k}\lambda'_{\varphi k} \\ \lambda'_{rk}\lambda'_{\varphi k} & \lambda'_{\delta k}\lambda'_{\varphi k} & \lambda_{\varphi k}^2 \end{pmatrix} + \sum_{k=1}^n \frac{w_{lk}w_{l'k}}{1+\gamma_k} \begin{pmatrix} 0 & \lambda'_{r\delta k} & \lambda'_{r\varphi k} \\ \lambda'_{r\delta k} & \lambda'_{\delta\delta k} & \lambda'_{\delta\varphi k} \\ \lambda'_{r\varphi k} & \lambda'_{\delta\varphi k} & \lambda'_{\varphi\varphi k} \end{pmatrix}, \quad (\text{A.8})$$

(b) concatenating $\bar{\mathbf{b}}_l''$ and $\bar{\mathbf{J}}_{ll}''$ for all $l, l' \in [0, N]$ to obtain the full \mathbf{b}'' and \mathbf{J}'' ,

(c) and advancing $\mathbf{r}_i = \mathbf{r}_{i-1} + \mathbf{J}''^{-1}\mathbf{b}''$, where $\mathbf{r} \equiv (r_0, \delta_0, \varphi_0, \dots, r_N, \delta_N, \varphi_N)^T$.

5. We repeat the two previous steps (steps 3 and 4) until $|\mathbf{r}_i - \mathbf{r}_{i-1}| < \varepsilon$ & $|L_i - L_{i-1}| < \varepsilon$, where ε is the “machine’s accuracy”, and $L = \sum_{k=1}^n \ln(1+\gamma_k)$.

References

- [1] T. Pospischil, [Aufbau und inbetriebnahme eines protonen-polarimeters an MAMI und messung der proton-polarisation in der reaktion \$p\(\vec{e}, e'\vec{p}\)\pi^0\$ in paralleler kinematik im bereich der \$\Delta\(1232\)\$ -resonanz](#), Ph.D. thesis, Institut für Kernphysik der Universität Mainz (2000).
URL <http://wwwa1.kph.uni-mainz.de/A1/publications/doctor/pospischil.pdf>
- [2] L. Doria, [Polarization observables in virtual compton scattering](#), Ph.D. thesis, Institut für Kernphysik der Universität Mainz (2008).
URL <http://wwwa1.kph.uni-mainz.de/A1/publications/doctor/doria.pdf>
- [3] A. A. J. DeGrush, [Single and double polarization observables in the electrodisintegration of the deuteron from blast](#), Ph.D. thesis, Massachusetts Institute of Technology (2010).
URL <https://dspace.mit.edu/bitstream/handle/1721.1/62644/713576977-MIT.pdf>
- [4] M. Paolone, Polarization transfer in ${}^4\text{He}(\vec{e}, e'\vec{p}){}^3\text{H}$, in: AIP Conference Proceedings, Vol. 947, AIP, 2007, pp. 182–185.
- [5] D. Besset, et al., [A set of efficient estimators for polarization measurements](#), Nucl. Instrum. Methods. Phys. Res., Sect. A 166 (3) (1979) 515 – 520. doi:10.1016/0029-554X(79)90543-3.
URL <http://www.sciencedirect.com/science/article/pii/0029554X79905433>
- [6] R. A. Fisher, Statistical methods for research workers, Genesis Publishing Pvt Ltd, 1925.
- [7] H. Merkel, et al., [Recoil polarization and beam-recoil double polarization measurement of \$\eta\$ electroproduction on the proton in the region of the \$S_{11}\(1535\)\$ resonance](#), Phys. Rev. Lett. 99 (2007) 132301. doi:10.1103/PhysRevLett.99.132301.
URL <https://link.aps.org/doi/10.1103/PhysRevLett.99.132301>
- [8] L. Doria, et al., [Measurement of the beam-recoil polarization in low-energy virtual compton scattering from the proton](#), Phys. Rev. C 92 (2015) 054307. doi:10.1103/PhysRevC.92.054307.
URL <https://link.aps.org/doi/10.1103/PhysRevC.92.054307>
- [9] S. Štajner, et al., [Beam-recoil polarization measurement of \$\pi^0\$ electroproduction on the proton in the region of the roper resonance](#), Phys. Rev. Lett. 119 (2017) 022001. doi:10.1103/PhysRevLett.119.022001.
URL <https://link.aps.org/doi/10.1103/PhysRevLett.119.022001>
- [10] G. Ron, The proton elastic form factor ratio $\mu_p G_E^p / G_M^p$ at low Q^2 , Ph.D. thesis, Tel Aviv University (2008).
- [11] G. Bohm, G. Zech, Introduction to statistics and data analysis for physicists, Vol. 1.
- [12] I. Yaron, D. Izraeli, et al., [Polarization-transfer measurement to a large-virtuality bound proton in the deuteron](#), Physics Letters B 769 (2017) 21 – 24. doi:10.1016/j.physletb.2017.01.034.
URL [sciencedirect.com/science/article/pii/S0370269317300527](https://www.sciencedirect.com/science/article/pii/S0370269317300527)
- [13] D. Izraeli, et al., Measurement of polarization-transfer to bound protons in carbon and its virtuality dependence, [arXiv:1711.09680](https://arxiv.org/abs/1711.09680).
- [14] T. Pospischil, et al., [The focal plane proton-polarimeter for the 3-spectrometer setup at MAMI](#), Nucl. Instrum. Methods. Phys. Res., Sect. A 483 (3) (2002) 713 – 725. doi:10.1016/S0168-9002(01)01955-6.
URL [sciencedirect.com/science/article/pii/S0168900201019556](https://www.sciencedirect.com/science/article/pii/S0168900201019556)
- [15] S. Strauch, et al., Polarization transfer in the ${}^4\text{He}(\vec{e}, e'\vec{p}){}^3\text{H}$ reaction up to $Q^2 = 2.6$ (GeV/c) 2 , Phys. Rev. Lett. 91 (2003) 052301. doi:10.1103/PhysRevLett.91.052301.

- [16] B. Hu, et al., Polarization transfer in the ${}^2\text{H}(\vec{e}, e'\vec{p})\text{n}$ reaction up to $Q^2 = 1.61 \text{ (GeV/c)}^2$, Phys. Rev. C73 (2006) 064004. doi : 10.1103/PhysRevC.73.064004.

